Photo-double-ionization of He: Fully differential and absolute electronic and ionic momentum distributions

R. Dörner,[1,*] H. Bräuning,[1,2,3] J. M. Feagin,[4] V. Mergel,[1] O. Jagutzki,[1] L. Spielberger,[1] T. Vogt,[1] H. Khemliche,[3] M. H. Prior,[3] J. Ullrich,[5] C. L. Cocke,[2] and H. Schmidt-Böcking[1]

[1]*Institut für Kernphysik, Universität-Frankfurt, August Euler Strasse 6, D60486 Frankfurt, Germany*

[2]*Department of Physics, Kansas State University, Manhattan, Kansas 66506*

[3]*Lawrence Berkeley National Laboratory, Berkeley, California 94720*

[4]*Department of Physics, California State University at Fullerton, Fullerton, California 92834*

[5]*Gesellschaft für Schwerionen Forschung, D64291 Darmstadt, Germany*

(Received 11 June 1997)

We measure fully differential cross sections for photo-double-ionization of helium at energies 1, 6, and 20 eV above threshold. The data have been obtained by measuring in coincidence the momentum vector of the He^{2+} ion and one of the electrons. Using time-of-flight and imaging techniques, we cover a solid angle of 25–100 % 4π of the final-state continuum of all particles. Therefore the experiment is not confined to any particular set of angles or energy sharing, and allows for a reliable absolute calibration. We present momentum distributions of the ions and a comprehensive set of differential cross sections for electron emission. The latter are *on an absolute scale* and cover both equal and unequal energy sharing—for both the fast and the slow electron fixed—and a wide range of polar angles. We also present the first data for noncoplanar geometry. For all energies the cross section is sharply peaked around the coplanar emission, i.e., both electrons are preferentially emitted in the plane of the recoiling ion and the photon polarization direction. For most of the geometries the shape of the cross sections is well described by fourth-order Wannier theory calculations. [S1050-2947(98)07802-0]

PACS number(s): 32.80.Fb

I. INTRODUCTION

Photo-double-ionization of helium is one of the simplest and hence most fundamental test cases for understanding many electron processes. It is in particular the dynamics of many-particle systems, as opposed to energy eigenvalues which are related to long time integrations, on which much of the recent work has focused. Dynamical electron correlation, visible for example in transitions of electrons to the continuum and momentum distributions in continuum states, is a rich puzzle that remains remarkably fragmented. Correlation effects determine the structure and evolution of our everyday world. They govern chemical reactions including basic biological systems. With the availability of new experimental techniques, one now has the opportunity to study fully fundamental many-body effects such as photo-double-ionization for the emergence of new phenomena at the transition from single-particle to multiparticle excitation.

In this paper we present absolute differential cross sections for He photo-double-ionization by linearly polarized light at 1, 6, and 20 eV above threshold for almost all polar and azimuthal electron-pair emission angles—coplanar and noncoplanar geometries—and for a wide range of electron energy sharings. Our results have been obtained using cold-target recoil-ion momentum spectroscopy (COLTRIMS). (For a recent review, see Ref. [1]; for applications of this technique to photoionization studies, see Refs. [2–5].) A few of the results of this experiment were presented in Ref. [4].

The key issues in the extensive literature on He photo-double-ionization can be grouped into three categories: (a) the He ground state, or initial-state correlation; (b) the three-body Coulomb continuum; and (c) bound-to-continuum transition mechanisms. These topics have been widely discussed, and even today remain far from closure. They have been addressed in two classes of experiments: (i) measurements of the ratio (R) of total double- and single-ionization cross sections as a function of photon energy [6–20,5,3,2]; and (ii) differential measurements of either the angular and energy dependence of one electron [19,21], or of both electrons in coincidence ($\gamma,2e$) [22–29].

Category (a). Long before the first ($\gamma,2e$) experiments became technically feasible, such investigations were proposed as a way to access the correlated atomic [30] and molecular [31] ground-state wave functions. Up until the present, highly sophisticated He wave functions have only been tested by the energy eigenvalues and decay rates they yield. For two-electron systems there is no analog to the one-electron Compton profile as it is observed in ($e,2e$) or Compton scattering experiments. Such an experiment would require the determination of conditional probabilities, for example the momentum distribution of one electron in the He *for a fixed momentum of the second electron* or the relative momentum between the two electrons in the bound state. It was originally hoped that ($\gamma,2e$) experiments might one day provide such information on bound states. This early goal has been mostly neglected in recent work on ($\gamma,2e$). It has, however, been addressed directly in recent advanced studies of double ionization by fast highly charged ion impact [32,33] and subsequent theoretical interpretations [34]. It is

*Electronic address: doerner@ikf.uni-frankfurt.de

thus one of the goals of the present work to provide a complete He photo-double-ionization dataset on an absolute scale, which might revitalize interest in the initial-state correlation. The connection between the measured final state and the initial state is, however, much more subtle than a Compton profile measurement, being masked by the transition process and the strong final-state correlation [35–37]. The role of the initial state will likely be revealed only by comparative theoretical studies [38].

In a fairly global fashion, initial-state correlation is addressed in the recent measurements of R by photoabsorbtion and by Compton scattering at asymptotically high energy. It was shown already by Byron and Joachain in 1967 [39] that at high photon energies the probability of ejection of the second electron depends on the initial state only, and that final state correlation may be neglected. The asymptotic value of R for photoabsorbtion and Compton scattering was settled experimentally only very recently [12–14,2,3,40]. Compared to fully differential cross sections this is only a crude test of the wave function. Total cross-section measurements nevertheless provide information on the ground-state wave function which is complementary to the energy eigenvalue. For example, the asymptotic value of R for photoabsorbtion proves to be sensitive to the portion of the ground-state wave function corresponding to only one very fast electron close to the nucleus.

Category (b). The character of the three-body continuum is shaped by the dynamical interaction among the three charged particles as well as by their total energy and angular momentum. The latter gives rise to characteristic nodal patterns in the angular distributions [41], and allows for a parametrization of the *fivefold* differential cross section (FDCS) [42,22,43,36]. Coulomb repulsion between the electrons has the most important consequences near threshold, where the three particles remain together longer. Kazanski and Ostrovski convincingly illustrated this formation of the asymptotic final state [44,45]. The dynamically favored threshold configuration of two equal energy electrons with antiparallel momenta is, however, forbidden by the $^1P^0$ symmetry. Thus the final-state momenta can only approach this Wannier configuration [46,42,47], with the consequence that the motion of the recoiling ion tends to freeze out, although zero ion momentum is again prohibited [4,48,49].

Category (c). The question of the mechanisms of photo-double-ionization has arisen mainly in work on R. (For a recent review, see Ref. [50].) While initial-state correlation (a) and final-state dynamics (b) are closely linked to experimentally accessible quantities, transition mechanisms are in general strongly theory-dependent concepts. They have been discussed for example in the framework of many-body-perturbation theory (MBPT). Here ''shake-off,'' TS1, or ''interception,'' and ground-state correlation are simply names for particular diagrams in the perturbation expansion. Following an argument by Dalgarno and Sadeghpour [51], Hino *et al.* showed that in MBPT the relative contributions of the different diagrams are gauge dependent [52]. This might be seen either as an indication of the limited use of the concept of mechanisms in general, or as a hint that MBPT diagrams are not good representations of our intuitively identified mechanisms in all gauges. One intuitive mechanism is revealed by the remarkably close proportionality of R as a function of photon energy to the single-ionization cross section for electron impact, found by Samson and co-workers [16,17]. This correspondence fails only at high energies, where it is necessary to assume an additional contribution from the shake-off mechanism.

One might expect that differential cross sections would show distinct structures which could be clearly attributed to reaction mechanisms. This expectation is unfortunately overshadowed by the presence of nodes or approximate nodes in the angular distributions due to final-state symmetries that place strong restrictions on the shape of the FDCS. In addition, the effect of final-state correlations at low photon energies seems to mask the signature of the ionization mechanism. Thus most investigations tended to explain the shape of the FDCS without explicit consideration of an ionization mechanism. However, Teng and Shakeshaft [53] and Pont and Shakeshaft [54] assigned emission angles near 90° between the electrons to the interception mechanism and angles of 0° and 180° to shake-off. Maulbetsch and Briggs [37] also attributed to shake-off their finding that, for very unequal energy sharing and 4-keV photon energy, the slow electron is nearly isotropic. Calculations of differential cross sections that could trace various mechanisms and even selectively switch them off would clearly be desirable. In the current work we add an additional element to the discussion by considering the momentum distribution of the recoiling He^{2+} ion. (See Ref. [4] for a brief overview.)

All three categories of questions (a)–(c) can be addressed by measuring the square of the final-state wave function in momentum space. This final state after photo-double-ionization of He is kinematically described by the nine momentum components of the three particles (two electrons and the recoiling nucleus). Due to energy and momentum conservation, only five momentum components are independent, and the corresponding FDCS fully describes the process of double ionization. At low energies the dipole approximation is expected to hold. In this case the linear momentum of the photon is neglected, yielding an additional rotational symmetry about the photon polarization axes. This results in a reduction from a fivefold to a fourfold differential cross section. In most of the work involving coincident electron detection, these cross sections are called ''triply differential,'' since they refer to the solid angles $d\Omega_1$ and $d\Omega_2$ of a pair of electron spectrometers as well as the energy E_1 of one of the electrons. (The energy of the other electron is fixed by the excess photon energy above the double-ionization threshold, $E_2=E-E_1$.) To measure such a cross section the experimentalist can freely choose which five out of the nine momentum components to measure. We have chosen to detect the components of the momentum vector (and charge state) of the ion together with the momentum components of one of the two electrons. Of these six measured momentum components, one is redundant.

Using electron-pair coincidence, Schwarzkopf and co-workers [22–24] placed one electron analyzer at a fixed angle and then moved a second one step by step. In an analogous fashion, Huetz and co-workers [25,27] employed a toroidal analyzer which accepts a range of polar angles for the second electron, while Viefhaus and co-workers [29,28] used time-of-flight electron analyzers which register a wide range of energy sharings. However, these coincidence experiments

detect at any given instant only an extremely small fraction of the three-body final-state continuum (on the order of 10^{-8}–10^{-5}). Thus these experiments are extremely difficult and time consuming.

By projecting both the ion and an electron onto wide-area position-sensitive detectors, we view 1π to 4π of the three-body continuum at once. Besides increasing the data collection rate tremendously, our approach has a substantial advantage regarding data analysis. The data are taken in event mode: for each single- or double-ionizing event we record the information necessary to determine the momentum vector of two particles. We are not required beforehand to decide what angles and energies to set our detectors. The dynamics of the physical process itself decides how every region of the five-dimensional momentum space will be populated. Thus we collect in a single continuous time period a comprehensive set of data covering all angles and energies. The data can then be sliced and sorted after the fact, indeed long after the experiment, in various ways without having to repeat the experiment. This is a common technique in many nuclear and particle-physics experiments, but is rare in photoionization studies.

We have thus obtained the first data for noncoplanar geometry with photon polarization out of the plane spanned by the momenta of the escaping electrons. The full coverage of the final momentum space allows one to represent the data in any set of coordinates, an advantage since some three-body properties of the final state prove more accessible in collective coordinates. We elaborated on this point in Ref. [4], and theoretically analyzed it in Ref. [48]. A further advantage of having a detector solid angle of almost 4π is that, since all the data are taken at the same time, the data are automatically normalized relative to each other, so that additional systematic error between the data is eliminated. In addition, it is straightforward to obtain an absolute normalization for the data, as we will show below. This absolute calibration is extremely difficult to achieve by coincident electron detection [24]. The absolute FDCS obtained in this work further contributes to the link between studies of R and the work on differential cross sections.

The FDCS for He was measured for the first time in a pioneering experiment by Schwarzkopf *et al.* [22] in 1993. In this and later experiments [23–25,27,26,28,29] the two electrons were detected in coincidence. These experiments illustrated in a striking way the constraints imposed on the shape of the angular distributions by the dipole-allowed symmetry of the final state, and its corresponding nodal structure. They demonstrated in addition the effect of repulsion between the two outgoing electrons. All these experiments however were restricted to coplanar geometry.

Three independent theoretical approaches have been successful in describing these measured cross sections. Angular distributions up to 20 eV above threshold were described by Wannier theory [47,46,42,55,44,56,45]. Although this theory predicts the relative photon energy dependence, it did not predict an absolute cross section. Maulbetsch and co-workers [35–37,41,57] used a final-state wave function formed by the product of three asymptotically correct Coulomb waves (3C), one for each pair of particles, to obtain relative FDCS, but they were not able to obtain reliable absolute cross sections. Pont and Shakeshaft employed screened Coulomb waves for each outgoing electron (2SC) and a numerically exact algorithm [58,54,49,59]. Their *a priori* calculations are unique in that they not only reproduced the shape of the FDCS but also predicted the absolute double ionization cross section and absolute recoil-ion momentum distributions in excellent agreement with experiment [58,5,49]. For the special case of equal energy sharing and coplanar geometry, agreement is found between all three theoretical approaches and available experimental data. For the general case of unequal energy sharing, however, substantial discrepancies between the 3C and 2SC approaches and with experiment are found [59], highlighting again the puzzling lack of understanding of one of the most basic few body problems in physics.

In Sec. II we give a brief description of our experimental setup. In Sec. III we describe our data analysis, and in Sec. IV A we present our results for single ionization to illustrate the technique of recoil-ion momentum spectroscopy. Finally, in Sec. IV B we present and discuss our results for double ionization including the momentum distributions of the recoil ions as well as the FDCS of the two electrons.

II. EXPERIMENTAL SETUP

The key to the present experiment is the realization of a spectrometer with 1π–4π solid angle for the coincident detection of two of the three fragments of the double-ionization event. This was realized by detecting the momentum vector of the ion and of one of the electrons. The technique of recoil-ion momentum spectroscopy has been developed over more than ten years, and is well established in ion-atom collision physics (see, for example, Refs. [60–70,32,33] and [1] for a recent review). At its heart are a localized internally cold target and wide-area position sensitive electron and ion detectors. An electric field guides the charged particles to the detectors and the momenta can be obtained from the time of flight and the position on the detector. The time-of-flight information of electron and ion are obtained from a coincidence of the respective detector signal with the machine pulse. The experiment was performed at beamline 7 of the Advanced Light Source at Lawrence Berkeley National Laboratory (LBNL). The ring was operated in double-bunch mode during this experiment to allow for such time-of-flight measurements.

The momenta of the ions expected in this experiment are in the range of a few atomic units (a.u.). Atomic units ($e=\hbar=m_e=\alpha c=1$) are used throughout this paper. The thermal motion of He at room temperature yields a momentum spread of the target atom of 4.3 a.u. Thus it is crucial for measurement of recoil-ion momenta to use an internally cold gas target. This was achieved by a precooled supersonic gas jet. A schematic of the scattering chamber with the jet system is shown in Fig. 1. The He gas expanded adiabatically through a nozzle of 30-μm diameter at a pressure of around 400 mbar. A gas reservoir and the nozzle were mounted on a cold finger and cooled to 29 K. From the preformed supersonic He gas jet the innermost part entered into the collision chamber through a skimmer of 0.3-mm diameter, mounted about 8 mm from the nozzle. The gas load from the expansion was pumped by one 220 l/s turbo molecular pump. This resulted in a He gas pressure of around 7×10^{-4} mbar in the expansion chamber. The helium gas jet was intersected with

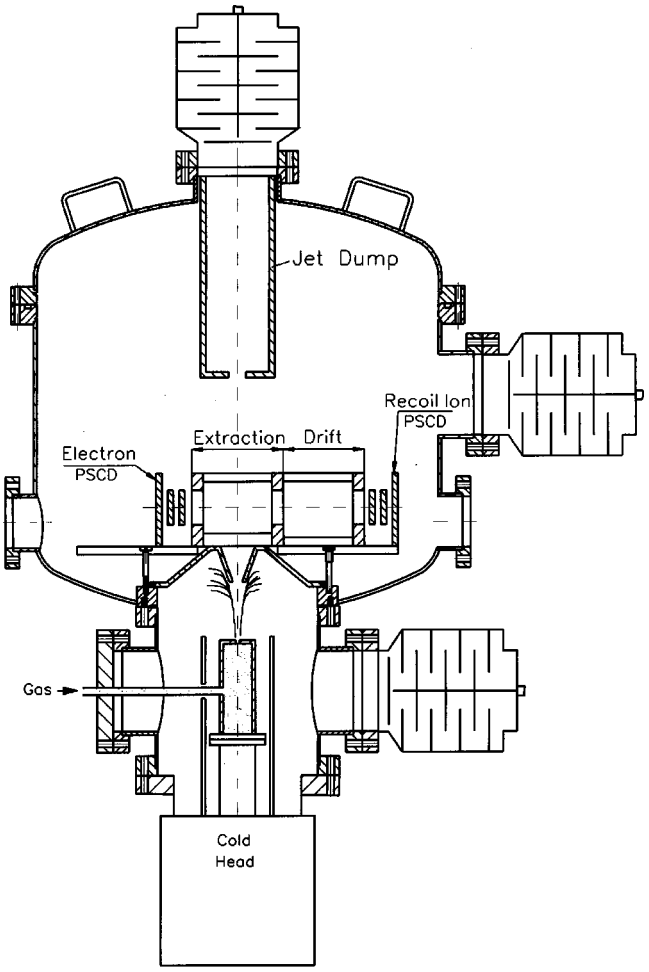

FIG. 1. COLTRIMS scattering chamber. The supersonic jet is produced in the source chamber (bottom), enters through a 0.3-mm-diameter skimmer into the scattering chamber (middle), and is dumped in the top. Each of the regions is pumped by a 220l/s turbomolecular pump. The gas nozzle is cooled to 29 K.

the photon beam at the focus of a mirror. At the interaction region the gas jet had a diameter of about 1.7 mm and a target density of several 10^{10} atoms/cm^2. The internal momentum spread of the gas jet in the two directions perpendicular to its direction of motion is defined by the gas jet velocity, and its divergence is obtained from the skimmer geometry. With the present setup we reached a momentum spread of ± 0.04 a.u. in the directions perpendicular to the jet. In the jet direction the momentum is given by $\sqrt{5kTm}$, with T being the nozzle temperature and m the mass of the gas atoms. This is only an offset velocity which does not harm the experimental resolution. The momentum spread around this offset momentum is given by the speed ratio. For the jet used here this momentum spread is smaller than in the perpendicular direction [71].

The spectrometer system used to detect electron and recoil-ion momenta is shown in Fig. 2. The ions and electrons created at the intersection region of the light with the gas jet are guided by an electric field toward two position-sensitive channel-plate detectors facing each other. Beamline 7 of the LBNL Advanced Light Source is specially designed for providing a very narrow beam. In the current experiment a focus of about 0.15 mm at the target was achieved. This small starting volume of $0.15\times0.15\times1.1$ mm^3 resulted in a very good momentum resolution for the ions and electrons.

For the present experiment an electric field of about 2.5 V/m in the target region was chosen. In the direction toward the electron detector a homogeneous acceleration field extended 1 cm to a grid of 0.25-mm mesh width followed by a 1-cm-long field-free drift region. From there the electrons pass a second grid and are postaccelerated by a potential of about 100 V onto a position-sensitive channel-plate detector with an active area of 48-mm diameter. The typical time of flight of a 0 eV electron is about 30 ns from the interaction region to the detector. An electron with 1.8-eV energy which starts perpendicular to the direction of the electric field reaches the detector at its edge. Thus the spectrometer has a 4π solid angle for electrons up to about 1.4 eV. The electron momentum vector is calculated from the position and the time of flight measured by a coincidence with the machine pulse.

The recoil ions are accelerated by an electric field over about 6 cm before they enter a field-free drift region of 30-cm length. A simulation of the electric field in the spectrometer together with some ion trajectories is shown in Fig. 3. The field acts as an electrostatic lens with focal plane on the channel plate detector. This improves significantly the momentum resolution in the two dimensions perpendicular to the field. Without the lens, the 1.7-mm diameter of the jet (i.e., the uncertainty in the starting point of the ion) restricts the momentum resolution. In the present setup, with a time of flight of about 12 μs for He^{1+}, 1.7 mm of jet diameter would result in a resolution of only 0.4 a.u. This restriction is overcome by the lens which focuses the ions from different starting positions onto the same position on the channel plate. Different starting momenta, however, still result in different trajectories. In the direction of the electric field a proper combination of field and drift regions is used such that ions at different starting points lead to the same time of flight. For a spectrometer with homogeneous fields, a first-order focusing in the time-of-flight direction is achieved by a ratio of 1:2 for acceleration to drift length; the insertion of a lens requires a longer drift tube to assure this focusing condition. The spectrometer shown in Fig. 2 realizes very good focusing conditions in all three spatial dimensions. For a more detailed description of the spectrometer, see Ref. [72]. Another crucial point is the use of narrow grids in front of the channel plate detector. The front side of the ion channel plate is at a potential of -3 kV. This is shielded by one grid with 80-μm mesh width from the field-free drift tube. The mesh width has been found to have significant effect on the resolution.

We used three time-to-amplitude (TAC) converters for the determination of the time of flight of the fragments. Two of which were started by the signals of the recoil ion or electron detector, respectively, and stopped by the machine pulse of the ring. A time range of 0.8 μs was used for this to achieve sufficient time resolution with an 11-bit analog-to-digital converter of 11 bit. The actual time resolution for both coincidences was found to be slightly better than 1 ns. The electron time of flight was much shorter than the time distance between the two bunches in the synchrotron. The ion time of flight, however, was much longer resulting in a

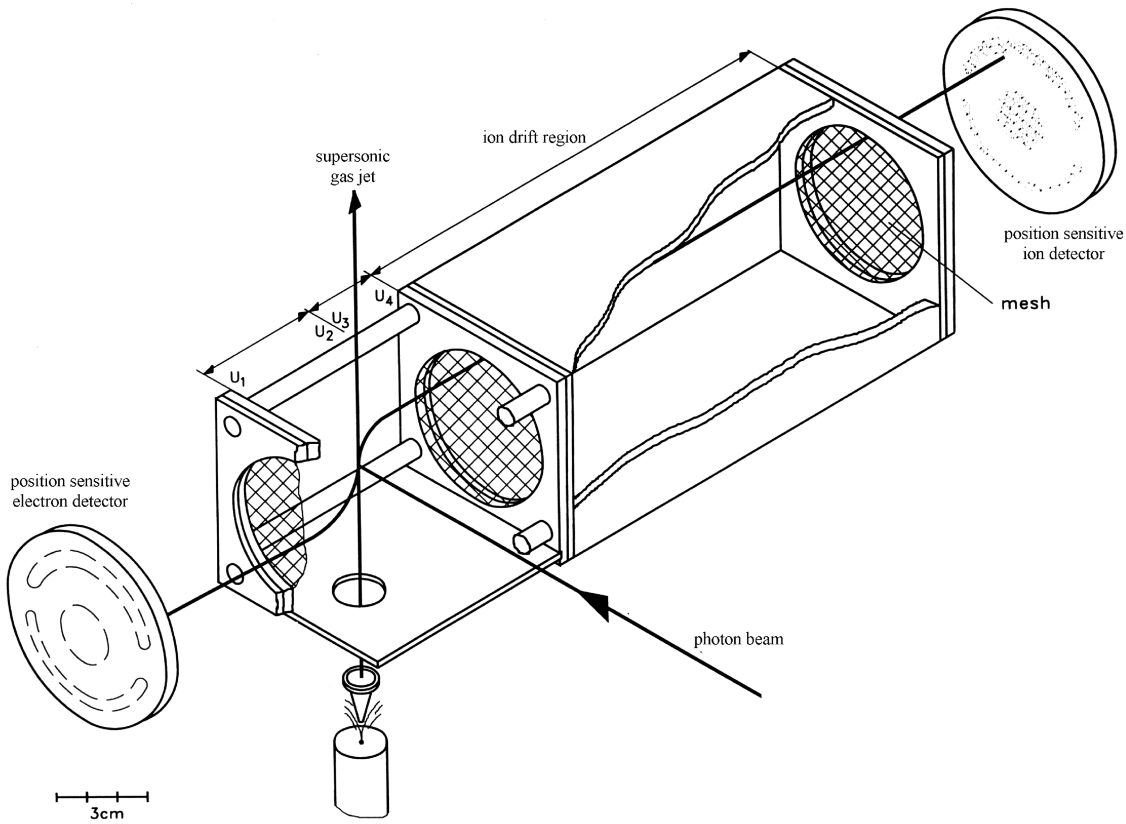

FIG. 2. Recoil-ion momentum spectrometer. The gas jet has a diameter of 1.7 mm at the intersection with the photon beam. The electrons are accelerated to the left, the ions to the right. Both detectors are *Z*-stack channel plate detectors, with an active area of 48-mm diameter and wedge-and-strip position readout.

''wrap around'' of the time-of-flight spectrum. The voltages were adjusted in a way that the He^{1+} and He^{2+} peaks in the spectrum did not overlap. The shape of the peaks for the He ions reflects their momentum distribution in the direction of the electric field and will be discussed in more detail in Sec. III. A third TAC was started by the electron signals and stopped by the ion signals, its information was used for selecting the real coincidence events. The raw spectra are shown in Fig. 4. All data are recorded in list mode. In addition to the time-of-flight information from the three TAC's, we recorded three pulse height signals from the wedge and strip anode of each of the two position-sensitive channel plate detectors for each event. A trigger (strobe signal) to read out the ADC is created for each He^{2+} ion and every eighth He^{1+} ion recorded in the ion-machine pulse coincidence. We obtained about 5000–10 000 He^{1+} ions per second. This resulted in a coincidence count rate of 4 s^{-1} for double-ionization events at 99-eV photon energy. All the data presented in this paper were taken in about 5–8 h data collection time per photon energy.

III. DATA ANALYSIS

A. Ion momentum measurement

In the off-line analysis we obtain the position information on the channel plate detectors for the electron and the ion from the pulse height signal of the three segments of the wedge-and-strip anodes which are recorded in list mode. Those events where both electrons hit the detector yield a false position information and are rejected using the pulse height of the signal. Figure 5 shows the position distribution of the ions on the channel plate detector. The ions have a maximum momentum determined by the photon energy. Since the spatial distribution on the channel plate is related

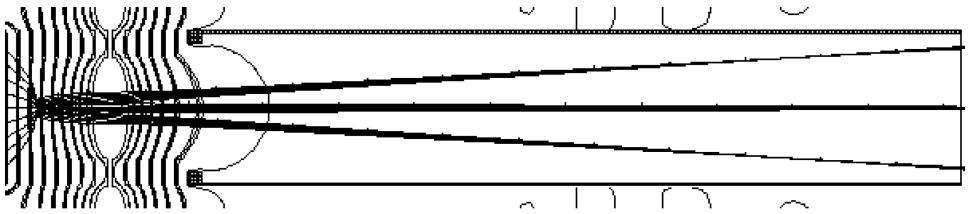

FIG. 3. Field geometry in the recoil-ion–electron spectrometer. The three groups of trajectories result from ions starting with different momenta in the direction perpendicular to the electric field.

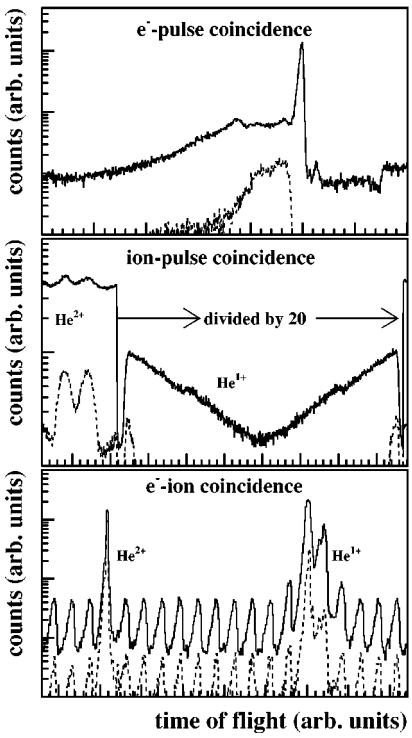

FIG. 4. Time-of-flight spectra. Upper: Time of flight (TOF) of electrons measured vs the bunch marker. The ring was operated in the double-bunch mode. The figure shows only one-half the spectrum (330 ns), belonging to one of the two bunches. The sharp peak results from single ionization. The dashed line shows the same spectrum gated on He^{2+} ions (in the lower spectrum). Middle: TOF of ions measured vs the bunch marker. The pulses in this TAC were used as the main event trigger. The data collection was always triggered if an event was within the indicated He^{2+} region, and only in one out of 20 events which fall into the indicated He^{1+} region. Again, only half of the spectrum [for one bunch (330 ns)] is shown. The dashed line shows the same spectrum gated on the spatial region of the detector where the He^{2+} ions hit. Lower: TOF of ions started with the electron signal. The structure in the background shows the bunch structure of the beam. The dashed line shows the spectrum gated as in the middle figure.

to the momentum distribution, in these two directions all ions have to fall within a circular area on this detector.

If the ion energy is small compared to the potential difference between the reaction volume and the drift region, the momentum $k_{\rm ion}^z$ of the ions in direction of the electric field is given by

$$k_{\rm ion}^z=(t-t_0)c_z, \tag{1}$$

where t is the actual time of flight of the ion, and t_0 is the time of flight of an ion with momentum zero. The proportionality constant $c_z=Uq$ depends on the electric field at the target U and the charge q of the ion only.

The momentum of the ion in the two directions perpendicular (x,y) to the extraction field for a spectrometer with homogeneous fields only, is given by

$$k_{\rm ion}^{x,y}=\frac{\Delta x,y}{t}m_{\rm ion}, \tag{2}$$

where Δx is the travel distance of the ion in the respective direction. This assumes that there is no component of the electric field along this direction. For the present spectrometer including an electrostatic lens (2) required modification of the calibration constants $c_{x,y}$. The three constants $c_{x,y,z}$ were obtained from the measured He^{1+} momentum distribution, discussed below.

B. Electron momenta

The electron momenta are obtained from the position on the channel plate and the time of flight similar to the procedure for the recoil ions. However the energy the ions receive from the electric field is much larger than their initial energy. Therefore the momentum in the TOF direction is in very good approximation linear to the time of flight [see Eq. (1)], and the TOF difference between those ions starting towards the ion channel plate and those which start in opposite direction is small compared to the total ion TOF. For the electrons this approximation does not hold. If the length of the acceleration and drift path and the electric field are exactly known, the momentum component in field direction can in principle be calculated from the measured TOF. However, to circumvent the uncertainties in the distance and voltage measurements, we calibrated the electron momenta using the measured recoil-ion momenta. The channel for a electron time of flight of zero was visible in the spectrum from a weak signal of photons from the decay of excited He^{1+}. In the two directions perpendicular to the electric field the electron momentum is proportional to the distance on the channel plate from the center and to the inverse time of flight. Again the calibration constant was obtained using the electrons coincident with He^{1+} ions. The resolution obtained is about 0.025 a.u. in the two directions perpendicular to the electric field (for electrons with less than 0.5 eV energy transverse to the field). In the direction measured by the time of flight the resolution is about 0.022-a.u. full width at half maximum (FWHM) at momentum zero, 0.05 a.u. at 0.3 a.u., and 0.16 a.u. at 1 a.u.

C. Analysis of the coincidence data

From the three (Cartesian) momentum components of the detected electron, $\mathbf{k}_1$, and the He^{2+} ion, $\mathbf{k}_{\rm ion}$, the momentum of the second electron, $\mathbf{k}_2$, was calculated for each event using momentum conservation (neglecting the photon momentum)

$$\mathbf{k}_2=-\mathbf{k}_{\rm ion}-\mathbf{k}_1. \tag{3}$$

The large amount of information recorded for each event allows for a very effective suppression of background from random coincidences. Figure 4 shows the time-of-flight coincidence spectrum between electron and recoil ions gated on the area on the recoil-ion channel plate detector where the He^{2+} ions hit the detector. It is this information on the ion time of flight which is, in terms of background suppression, the major advantage of an ion-electron coincidence compared to an electron-electron coincidence.

In order to compare our data with those obtained by traditional coincident electron spectroscopy, we present the angular distributions of one electron for fixed energy and angle

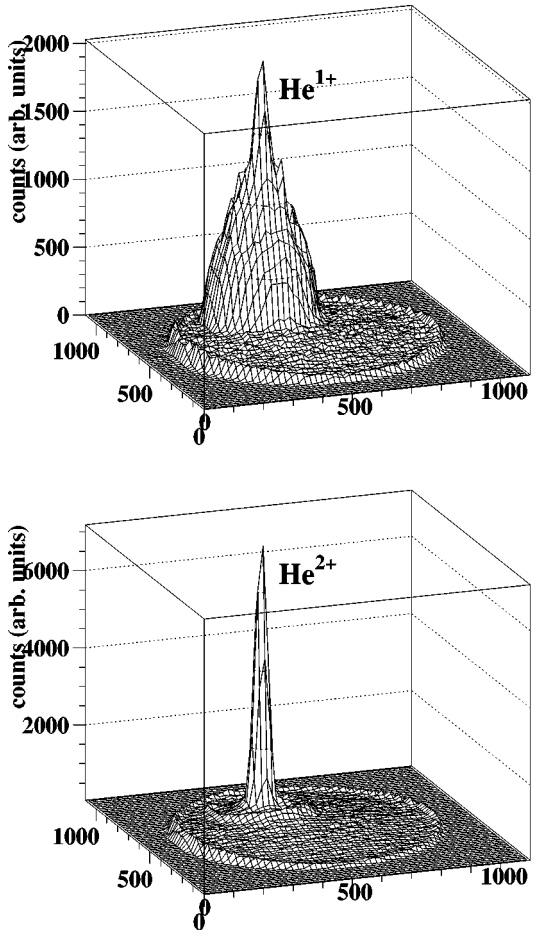

FIG. 5. Spatial distribution of recoil ions on the channel plate detector. Upper figure: gated on He^{1+} ions in the time of flight; lower figure: gated on He^{2+} ions.

of the second electron. We show data for an excess energy of 1, 6, and 20 eV. To obtain the best possible resolution with our setup, we used the subset of data where the slower electron is detected by our electron detector, and the momentum vector of the fast one is calculated using the ion momentum.

In the dipole approximation the double-ionization process has rotational symmetry around the polarization axis of the linear polarized light. Thus all cross sections depend on the azimuthal angle between the two electrons only, and not on the azimuthal angle in the laboratory frame. We have therefore sorted our data with respect to the azimuthal angle between the two electrons only, and integrated over the laboratory azimuthal angle of all particles.

D. Absolute calibration

At 80-eV photon energy and therefore 1-eV excess energy, our spectrometer spans the full 4π solid angle for all three particles. In this case, the absolute calibration is straightforward: the total number of counts obtained corresponds to the total cross section. We normalized our data to the total cross section of Ref. [75] of 1.11 10^{-21} cm^2. We should emphasize that with this normalization procedure the total photon flux, the detection efficiency, the gas target pressure, the instrumental resolution and data acquisition dead times do not affect the calibration. The only uncertainties result from the total cross section and the accuracy of the energy and angular gates used for the electron, which is held fixed for generating the FDCS. Our error on absolute scale at 80 eV is smaller than 20%, and the additional statistical error is indicated by the error bars.

For 85- and 99-eV photon energies, we have full solid angle only for electrons with less than 1 eV energy. We interpolate to the full cross section by assuming a flat electron energy-sharing distribution. This is in agreement with the measurement of Wehlitz *et al.* within their errors [19] and for 99 eV in excellent agreement with the calculations of Proulx and Shakeshaft [73]. We then normalized to the total photoionization cross section of Samson *et al.* [74] and a ratio of double to single ionization of 0.66% at 85 eV and 2.28% at 99 eV which were measured with our apparatus [5]. The overall error in this absolute calibration consists of the error in the assumption of a flat energy distribution (estimated $<15\%$), the total photoionization cross section (2% [74]), and the ratio (6%). An additional error results from nonlinearities of our system. For all data with unequal energy sharing, in order to cancel our energy nonlinearities, we gated the differential spectra on the same energy range which was used for the calibration. For the data with equal energy sharing we estimate this effect to be 30%. Thus the total uncertainty in the absolute calibration of our data at 85 and 99 eV is 16% for unequal energy sharing, and 34% for equal energy sharing.

IV. RESULTS AND DISCUSSION

A. Single ionization

From energy and momentum conservation, the momentum $k_{He^{1+}}$ of the He^{1+} ions is given by

$$k_{He^{1+}} = \sqrt{2(E_\gamma - E_{exc} - E_{bind})}, \tag{4}$$

where E_{bind} is the ionization potential of the He atom and E_{exc} is the internal excitation energy of the residual He^{1+} ion. For the current experiment the photon momentum (0.027 a.u. at $E_\gamma = 100$ eV) and the ion energy (<11 meV) can be neglected. For single ionization the ion therefore compensates almost exactly the momentum of the electron. In momentum space all He^{1+} ions are located on spheres around the origin. This has been exploited to obtain the calibration constants and the times of flight and positions for ions with momentum zero (which is the center of the time of flight and spatial distributions). Figure 6 shows a slice through the He^{1+} momentum distribution. Rings from the excited states of the He^{1+} can be seen. A traditional electron spectrometer with electrostatic deflectors would measure only one point of this plot at a time. A time-of-flight spectrometer measures the intensity distribution along a radial line from the origin (which is in a given solid angular range Ω at a polar angle ϑ and azimuthal angle Φ). Due to the projection of the ions with 4π solid angle onto the detector, the current setup records the spheres at the same time with a rate of several thousand events per second.

The probability distribution on the outer ($n=1$) sphere reflects the degree of linear polarization of the light and the β parameter of the reaction channel. Within the dipole approximation the angular distribution of the electrons and thus

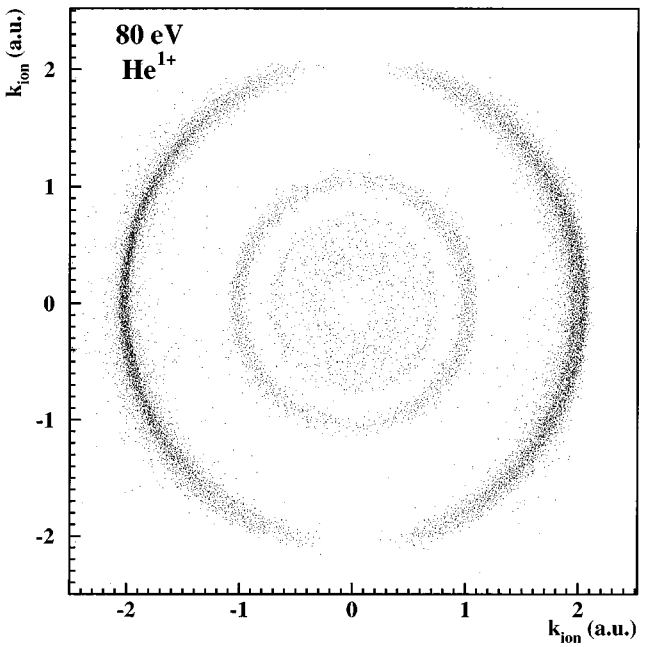

FIG. 6. Slice through the three-dimensional momentum distribution of He^{1+} ions from 80-eV photons. The electric-field vector is along the x axis. The smaller rings result from ions in excited states.

the ions as a function of the polar angle ϑ with respect to the direction of the electric field vector and the azimuthal angle ϕ around this axis is given by [76]

$$\frac{d^2\sigma(\vartheta,\phi)}{d\Omega}=\frac{\sigma}{4\pi}\{1+\beta[\tfrac{3}{4}(1-\sin\phi^2\sin\vartheta^2+S_1\cos\vartheta^2 -S_1\cos\phi^2\sin\vartheta^2)-\tfrac{1}{2}]\}. \quad (5)$$

In the case of the Stokes parameter $S_1=1$ (fully linear polarized light), the equation simplifies to

$$\frac{d^2\sigma(\vartheta,\phi)}{d\Omega}=\frac{\sigma}{4\pi}[1+\beta(\tfrac{3}{2}\cos\vartheta^2-\tfrac{1}{2})]. \quad (6)$$

For the transition to the $He^{1+}(n=1)$ ground state, the spin of the photon results in $\beta=2$. Figure 7 shows the probability distribution of the He^{1+} ion as a function of their momentum integrated over all angles. From this the overall resolution of the apparatus can be determined to ± 0.07 a.u. This results to some extent from the nonlinearity of the system. The dashed line shows the distribution integrated only over a polar angular range of $\vartheta=0°-10°$, reflecting the local resolution of the system of ± 0.045 a.u. Figure 8 shows the distribution of the ions as function of the cosine of the polar angle integrated over all azimuthal angles. From a fit to this spectrum one obtains the Stokes parameter of the light used in the current experiment to be $S_1=0.99\pm 0.01$. For single-ionization plus excitation to the $n=2$ state (Fig. 8), we obtain $\beta=0.86\pm 0.02$ at 85 eV, which is within the scatter of the experimental data from Refs. [77–79].

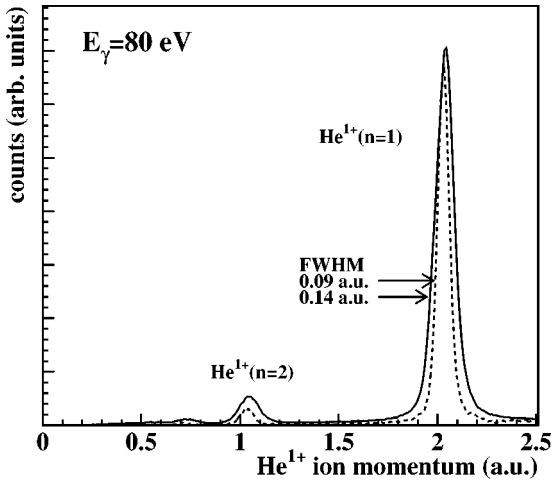

FIG. 7. Momentum distribution of He^{1+} ions created by 80-eV photons. The full line is integrated over all polar and azimuthal angles (integrating over all small nonlinearities of the system). The dashed line is for a polar angle of $0°-10°$ (scaled to match the maximum).

B. Double ionization

The double-ionization continuum in general is described by a probability distribution in a five-dimensional momentum space. As outlined in Sec. I, this five-dimensional space has at least one symmetry within the dipole approximation. This rotationally symmetry around the polarization direction of the light allows a reduction to four dimensions. Out of the many perspectives one might look at these four dimensions we first discuss the momentum distribution of the He^{2+} ions (which implies an integration over two out of four dimensions) and, second, electron angular distributions for fixed direction and energy of the other electron as they would be obtained from experiments by coincident electron detection.

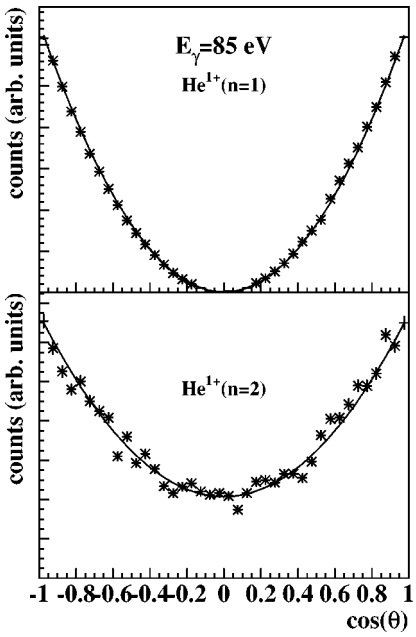

FIG. 8. He^{1+} count rate vs cosine of the polar angle with respect to the polarization axis, integrated over all azimuthal angles. The fit to the ground state shows a Stokes parameter of $S_1=0.99\pm 0.01$. The best fit to the $n=2$ results is $\beta=0.86\pm 0.02$.

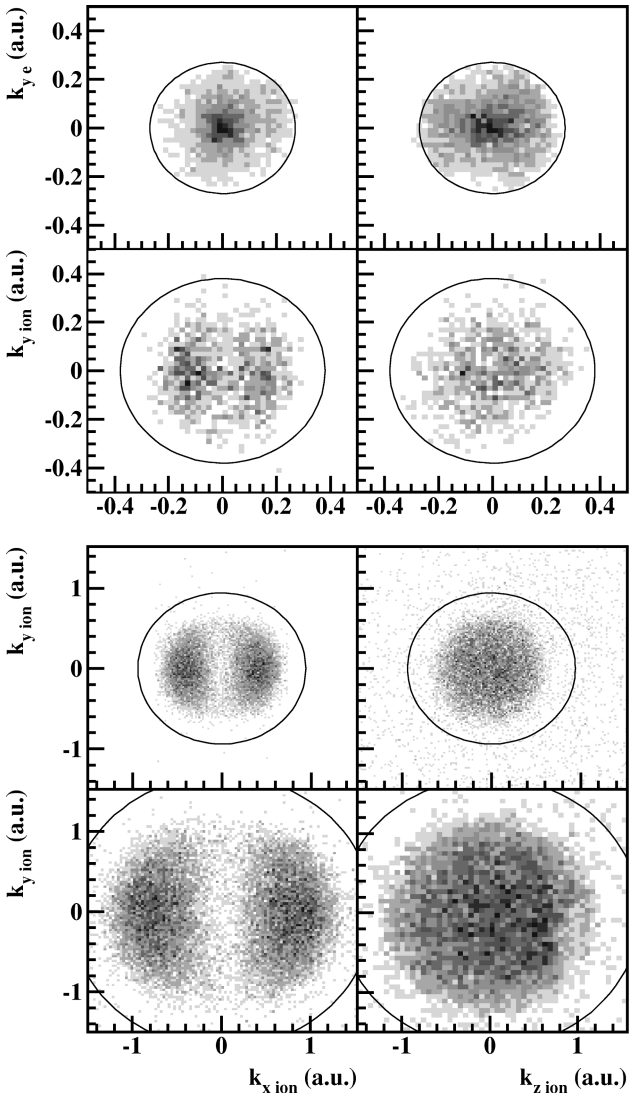

FIG. 9. Momentum distribution of electrons and He^{2+} ions from photons with 1-, 6-, 20-eV excess energy. *X*: direction of polarization; *Y*: direction of photons propagation; *Z*: perpendicular to both. Left column: plane of electric field vector and photon propagation. Right column: plane perpendicular to the polarization axis. First row: Distribution of one electron (1 eV above threshold). Second row: He^{2+} ions, 1 eV above threshold. Third, fourth row: He^{2+} ion 6 and 20 eV above threshold. The circle indicates the maximum possible momentum.

1. Ion-momentum distributions

Fully equivalent to the case of single ionization, Fig. 9 shows the momentum distribution of the ions for double ionization. Since the two electrons in the continuum can share the excess photon energy and emerge with various relative angles, the ion momenta are no longer restricted to spheres in momentum space. The maximum ion momentum at a given photon energy is

$$k_{\text{ion}} = 2\sqrt{(E_\gamma - E_{\text{bind}})}, \tag{7}$$

where E_{bind} is the sum of the ionization potentials for both electrons. This momentum, which is indicated by the circle, corresponds to the situation where both electrons escape with equal energy in the same direction. As already shown in Ref.

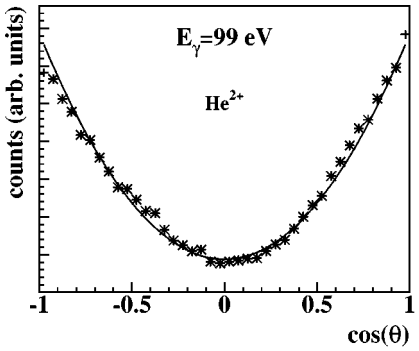

FIG. 10. As in Fig. 8 but for He^{2+} ions from 99-eV photons.

[22], this is inhibited by the electron-electron repulsion, and thus the cross section falls to zero toward the circular line. The left column of the figure shows the projection of a slice in momentum space onto a plane spanned by the photon propagation axis and the polarization vector; the right column shows a projection onto the plane perpendicular to the polarization. The distribution is rotationally symmetric around this axis. The cross section again has a node at zero ion momentum. This corresponds to the case of both electrons emerging with equal energy in opposite directions. As shown by several authors, this is prohibited by a selection rule [22,35,43].

As for the electron emission (integrated over the second electron and the ion), so the angular distribution of the ion can by parametrized for fully linear polarized light according to Eq. (6). Thus, as shown recently by Feagin [48] and Pont and Shakeshaft [49], the angular distribution for each ion momentum can be described by one parameter $\beta_{\text{ion}}(k_{\text{ion}})$. For illustration, Fig. 10 shows the angular distribution of the He^{2+} ions at 99-eV photon energy with a fit according to Eq. (6). The β parameters which can be extracted this way from the data shown in Fig. 9 can be found in Ref. [4]. Our ion-momentum distributions as well as the β parameters are in very good agreement with the *a priori* calculations by Pont and Shakeshaft [49] and calculation in fourth-order Wannier theory [4,48].

It is instructive to compare the ionic momentum distributions to those of electrons. At energies below 100 eV the electronic β parameter is found to be close to zero, or at low energies even negative [19,21,4]. The energy distribution is almost flat. For comparison with the ionic momentum distributions we have displayed this known electronic distribution in Cartesian momentum coordinates for 1-eV excess energy (first row of Fig. 9). The striking difference between the electronic and ionic distributions invites speculation on the mechanisms of photo-double-ionization. The photon acts upon a charge dipole in the atom. This dipole might be thought of as consisting of the positive ion on one pole and either the center of charge of the electron pair or one of the electrons on the other pole. In either case the first step of the absorption of the photon will imprint the dipolar characteristics of the linear polarized photon on the distribution of the fragments of a charge dipole. The experiment indicates that the momentum distribution of the nucleus shows a memory of this absorption of the photon, while it is completely smeared out in the electron momentum distribution. If one

favors the electron pair as the ion's counterpart in the photon-absorbing charge dipole, the subsequent breakup motion of the electron pair is mainly responsible for the electron distribution. The direction of this breakup given by the electron-pair relative momentum $\mathbf{k}_R=\frac{1}{2}(\mathbf{k}_1-\mathbf{k}_2)$ has been found for 1-eV excess energy to be mainly perpendicular to the photon polarization axis. For additional discussion, see Refs. [4,48]. The picture of such a collective motion of the electron pair is most plausible close to threshold. At higher photon energy it seems more appropriate to think of a (single electron + ion dipole) absorbing the photon. Of course, then electron correlation is indispensable to double ionization. One concludes that it is this electron-electron interaction which smears out the observed recoil-ion dipole pattern. This point of view is in qualitative agreement with the model of Samson and co-workers [16,17] which views photo-double-ionization as photoabsorbtion by one electron followed by internal electron-impact ionization.

For the description of electron-pair continua and bound states, molecular Jacobi coordinates have proven useful [80,47,48]. Besides the relative momentum of the electron pair $\mathbf{k}_R=\frac{1}{2}(\mathbf{k}_1-\mathbf{k}_2)$, one introduces the momentum of the pair's center of mass $\mathbf{k}_r=\mathbf{k}_1+\mathbf{k}_2$, the latter being equal and opposite to the recoil-ion momentum, $\mathbf{k}_{\rm ion}=-\mathbf{k}_r$. These coordinates also invite a change in perspective toward the double-ionization process. With the electronic coordinates $\mathbf{k}_{1,2}$, the two electrons are thought of as escaping from a central potential created by the ion and some portion of the electron-ion interaction with the electron-pair repulsion shaping the angular distribution of the electrons. The Jacobi momenta naturally describe on the other hand the motion of the ion in the two center saddle potential of the electron pair. In Ref. [4] we showed that for 1-eV excess energy the inter-electronic axis is oriented preferentially perpendicular to the electric field vector. Thus the ions shown in Fig. 9 escape from the saddle preferentially along the stable direction. In Wannier theory this preferred motion is related to a state with angular-momentum projection $\mathbf{L}\cdot\hat{\mathbf{k}}_R=K$ along a body-fixed axis $\mathbf{k}_R$ [48,4]. Lablanquie *et al.* [27] and later Viefhaus *et al.* [28] also argued for preferred population of the $K=1$ states close to threshold from an analysis of their electron angular distributions. They found the contribution of their a_u amplitude [see Eq. (8) below] to be typically smaller than $\frac{1}{19}$ of the a_g amplitude at 4-eV excess energy. In addition to the orientation of the saddle, an analysis of the partitioning of the excess energy between the breakup motion of the electron pair and its center-of-mass motion shows that the ion tends to freeze out on the saddle as the photon energy approaches threshold. A determination of the ion-momentum distribution for fixed orientation of the interelectronic axis is the subject of a new experiment, and will be discussed in a forthcoming paper.

2. FDCS for electron emission

Following the work performed by coincident electron detection, we now choose as coordinates the energy E_1 of one electron, the polar angles ϑ_1 and ϑ_2 of the two electrons with respect to the photon polarization axis and the azimuthal angle ϕ between the two electrons. The energy of the second electron is then fixed by $E_2=E_\gamma-E_{\rm bind}-E_1$, where

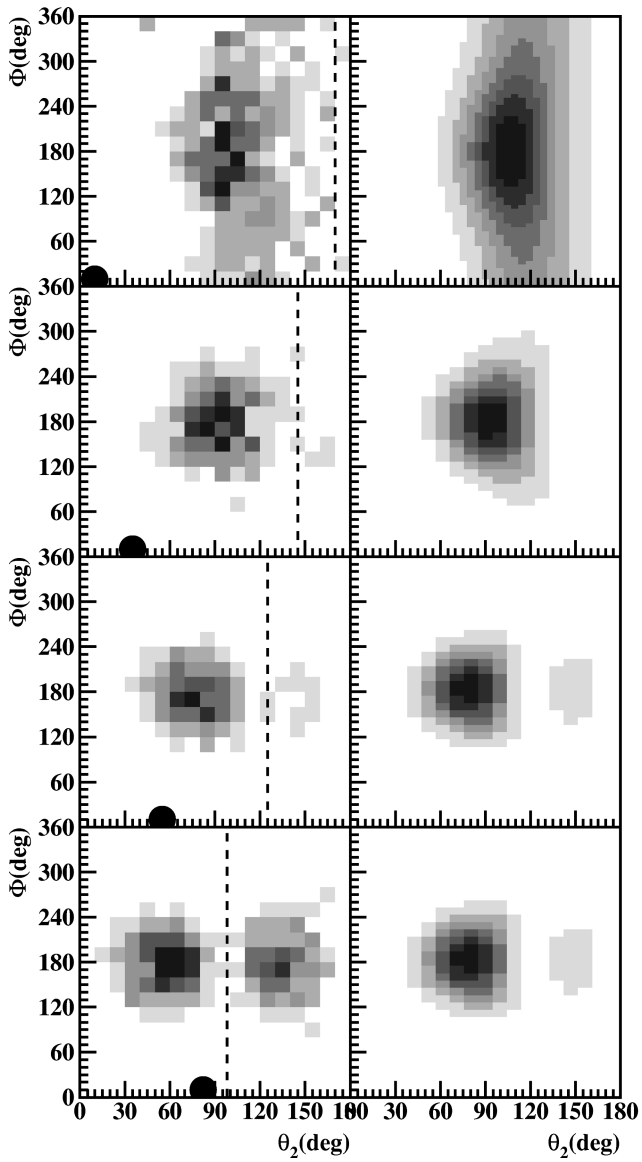

FIG. 11. $d^4\sigma/d\vartheta_1 d\vartheta_2 dE_1 d\Phi$. Horizontal axis: ϑ_2; vertical axis: azimuthal angle between both electrons. $E_\gamma=85$ eV; the energy of the fixed electron is $E_1=0.1$–1 eV. $\vartheta_1=0°$–$20°$, $\vartheta_1=30°$–$40°$, $\vartheta_1=50°$–$60°$, $\vartheta_1=75°$–$90°$ (from top to bottom). The direction of the fixed electron is indicated by the dot. The dashed line shows the location of the node for the case of equal energy sharing (see text). Left column: experiment; right column: fourth-order Wannier calculations.

$E_{\rm bind}$ = 79 eV is the electron-pair binding energy. Thus the FDCS is given by $d^4\sigma/d\cos\vartheta_1 d\cos\vartheta_2 dE_1 d\phi$. For a qualitative overview on the correlated electron emission pattern at an excess energy of 6 eV we show two-dimensional representations of the FDCS for fixed ϑ_1, E_1 as a function of ϕ and ϑ_2 (Fig. 11). For a more quantitative discussion we then turn to one-dimensional polar representations of the FDCS. We illustrate the effect of the excess energy for the case of equal energy and coplanar geometry (Fig. 12), then turn to the discussion of noncoplanar geometries (Fig. 13), then to the effect of the energy sharing on the FDCS (Fig. 14), and finally illustrate a node in the cross section for both electrons emitted perpendicular to the polarization axis (Fig. 15).

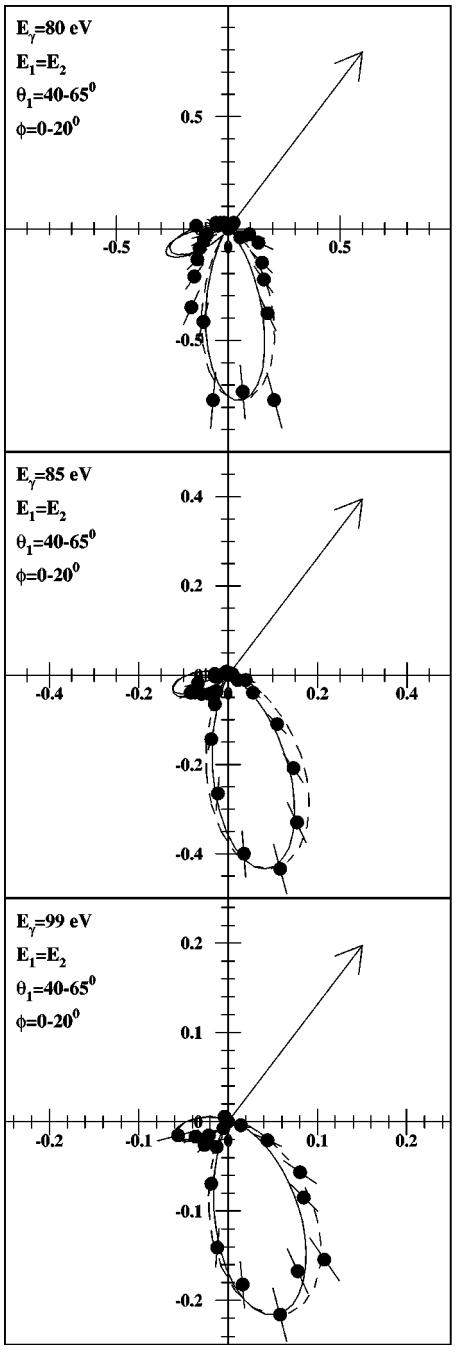

FIG. 12. $d^4\sigma/d[\cos(\vartheta_1)]d[\cos(\vartheta_2)]d\phi\, dE$ for photon energies of 80, 85, and 99 eV for equal energy sharing. The first electron is emitted in a polar angular range $\vartheta_1 = 40° - 65°$. The azimuthal angle between the two electrons is $180° \pm 20°$. The dashed line indicates a fit with a Gaussian correlation function with the FWHM as given in Table I. The fit function was integrated over the polar and azimuthal opening angle given above. Full line: fourth-order Wannier calculation. The polarization axis is horizontal. The data are on absolute scale in 10^{-4} a.u., the error bars represent the statistical error, the additional systematical error is discussed in Sec. III D, and the lines are scaled to the data.

Figure 11 shows the evolution of the angular distribution of the second electron for unequal energy sharing for the angle ϑ_1 varying from 0° to 90° with respect to the polarization axis. The energy of the first electron is selected to be between 0.1 and 1 eV (thus the second electron between 5 and 5.9 eV). The gray scale of the figure is linear in the cross section $d^4\sigma/d\vartheta_1 d\vartheta_2 dE_1 d\Phi$. The count rate in our spectrometer is, contrary to coincident electron detection, proportional to $d\vartheta_1 d\vartheta_2 d\phi \sim d\Omega_1 d\Omega_2/\sin\vartheta_1 \sin\vartheta_2$. In all of the following figures, we therefore plotted $d\sigma/d\cos\vartheta_1 d\cos\vartheta_2 d\phi dE_1$, i.e., we multiplied our original data (as displayed in Fig. 11) by $\sin\vartheta_1 \sin\vartheta_2$ for better comparison with other published data. Figure 11 demonstrates that at all angles ϑ_1 the FDCS is maximum for $\phi = 180°$. This corresponds to the coplanar geometry to which all experiments so far have been confined. The emission of the second electron changes from a cone for ϑ_1 close to 0° to one main lobe in the intermediate range of angles, which turns with ϑ_1. (There is a second very small lobe which is not visible in this presentation but is visible in the one-dimensional presentation below.) Finally, a second lobe grows as 90° is approached.

It has been pointed out by several authors [42,22,41,43] that the FDCS's are governed by strict selection rules, especially in the case of equal energy sharing. Already in the first $(\gamma,2e)$ experiment on He, Schwarzkopf *et al.* [22] saw a node for antiparallel electron emission resulting from the $^1P^0$ character of the final state. Maulbetsch and Briggs [41] showed that for equal energy sharing there is also a node at $\vartheta_2 = 180 - \vartheta_1$ [selection rule (F)]. We mark the location of this cone with a line in Fig. 11. For unequal energy sharing this selection rule does not hold strictly. At 6-eV excess energy, however, the selection rules still seem to govern the process for an energy sharing of $\frac{1}{5}$. This is in agreement with the observations of Lablanquie *et al.* for the special case of coplanar geometry $(\phi = 0)$ and $\vartheta_1 = 0$.

Huetz and co-workers [42,43] suggested interpreting the cross sections from a parametrization of the FDCS. They have shown that within the dipole approximation the FDCS can be written as

$$\frac{d^4\sigma}{dE_1 d\cos\vartheta_1 d\cos\vartheta_2 d\phi} \sim |(\cos\vartheta_1 + \cos\vartheta_2) a_g(E_1, \vartheta_{12}) + (\cos\vartheta_1 - \cos\vartheta_2) a_u(E_1, \vartheta_{12})|^2, \tag{8}$$

with two arbitrary complex functions a_u and a_g of the angle between the two electrons ϑ_{12} and the energy sharing. The amplitude a_u is antisymmetric under exchange of the electrons so that $a_u = 0$ for $E_1 = E_2$. With the additional but reasonable assumption of a_u and a_g being smooth functions of ϑ_{12}, the selection rules can be deduced immediately from this parametrization. The advantage of this approach is that it splits the cross section into a trivial part which describes the symmetry of the $^1P^0$ state and two functions of lower dimension which describe the three-body dynamics. Recently Malegat and co-workers [43] proposed a further analysis of the two amplitudes in terms of bipolar harmonics. Feagin achieved a similar parametrization of the cross section in the Jacobi coordinates discussed in Sec. IV B 1 [48]. The function $|a_g|^2$ was modeled with some success by a Gaussian peaked at 180° [22,25,81,49]. Kazanski and Ostrovski illustrated within a restricted Wannier model how $|a_g(\vartheta_{12})|^2$ evolves toward a narrow peaked function centered at $\vartheta_{12} = 180$ with increasing distance between the particles in

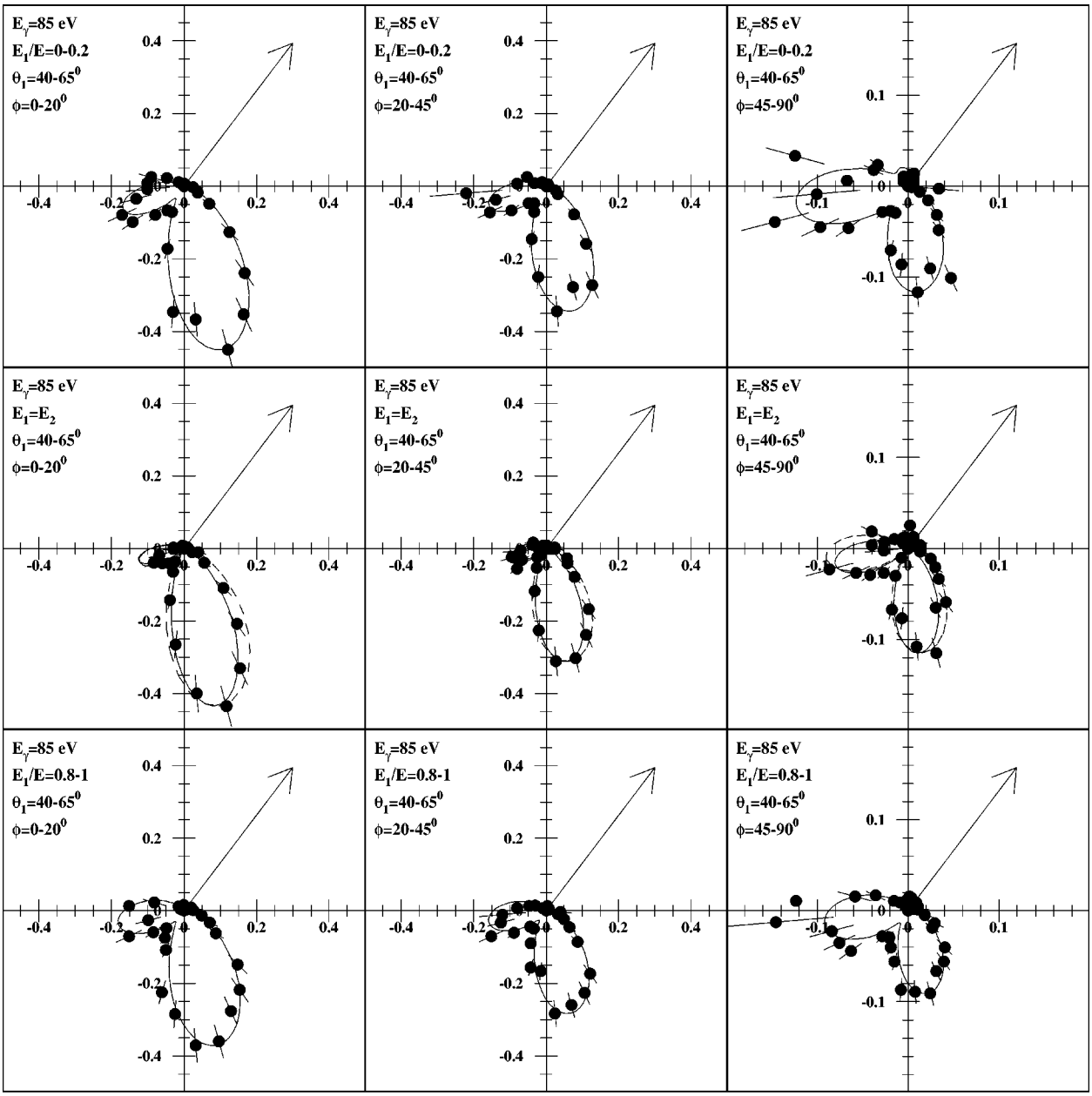

FIG. 13. $d^4\sigma/d[\cos(\vartheta_1)]d[\cos(\vartheta_2)]d\phi\,dE$ for a photon energy of 85 eV. The first electron is emitted in a polar angle range of $\vartheta_1 = 40° - 65°$. Each row is for a different energy sharing, each column for varying azimuthal angle between the two electrons as given in the figure. The dashed line shows a fit with a Gaussian correlation function with the FWHM equal to 84.7°. Full line: fourth-order Wannier calculation. The data are on absolute scale in 10^{-4} a.u.; the lines are scaled to the data.

the breakup. Even within the Wannier description the correlation function is, however, not necessarily a Gaussian [55].

For illustration of Eq. (8) and comparison with all other $(\gamma,2e)$ experiments, we fitted all our data for equal energy sharing and as function of ϑ_1, ϑ_2, and Φ by Eq. (9) assuming

$$|a_g(\vartheta_{12})|^2 = Ae^{-(\vartheta_{12}-180)^2/2\sigma_w}. \quad (9)$$

We fitted our data for 1-, 6-, and 20-eV excess energy. The fit was performed on a coplanar subspace of our data and to the region of ϑ_1 for which we have full acceptance. The azimuthal angle on the dataset has been restricted to $\pm 20°$ out of the coplanar plane. To account for the effect of this opening angle, we also integrated the fit over the identical azimuthal angle. As a cross check on the fit parameters we also fitted measured distributions of the FDCS for fixed ϑ_1 as a function of ϑ_2 and ϕ, as they are shown in Fig. 11. Again for those fits the opening angle for ϑ_2 was included in the fit via integration. Within the given errors the fits on the different subspaces of the experimental data yielded the same result. Table I shows the fitted FWHM together with comparable values from the literature. Our results are in very close agreement with the results of all other studies. We include lines calculated with our fit parameters in all further figures for comparison.

The figures also show results from a fourth-order Wannier description [47] used originally in an analysis of the recoil-

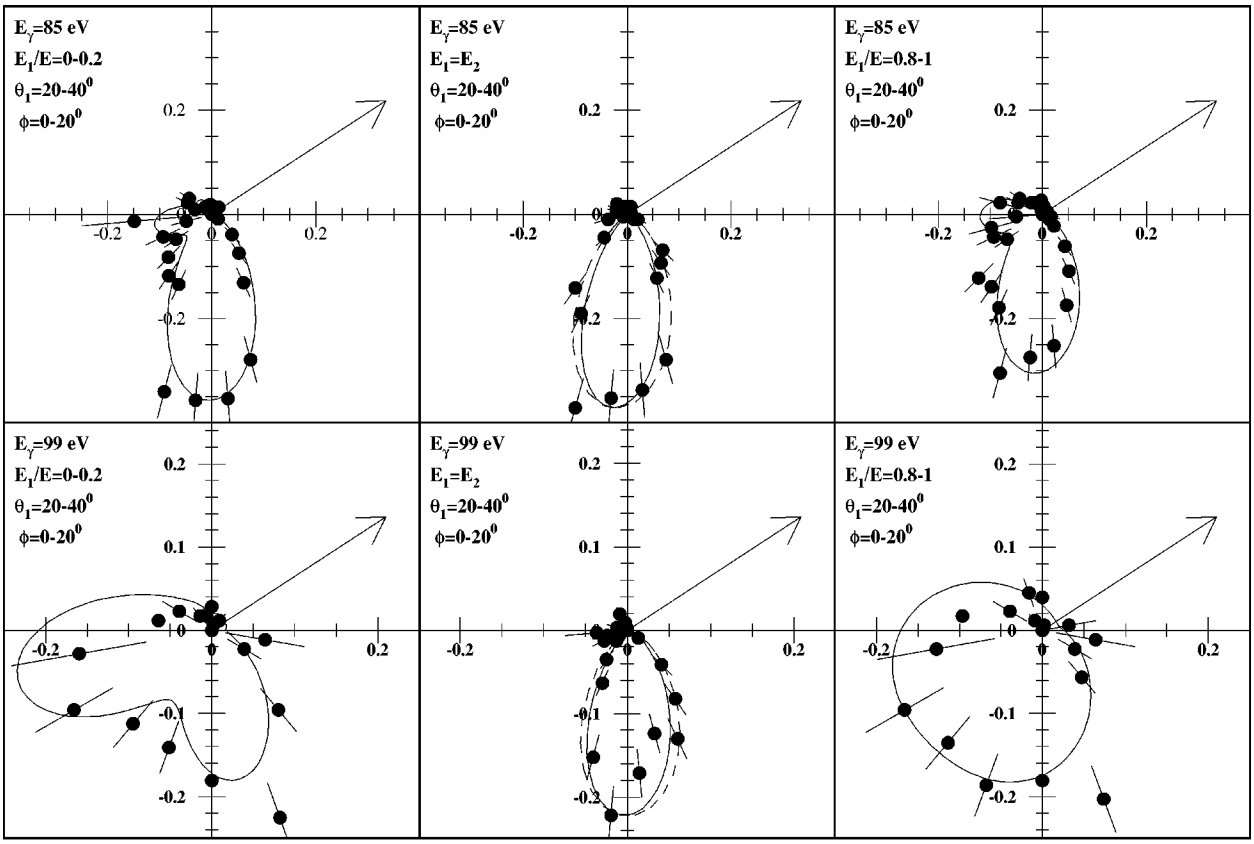

FIG. 14. $d^4\sigma/d[\cos(\vartheta_1)]d[\cos(\vartheta_2)]d\phi\, dE$ for photon energies of 85 and 99 eV. Angles and energies as given in the figure. The dashed line shows a fit with a Gaussian correlation function with a width as given in Table I. Full line: fourth-order Wannier calculation. The data are on absolute scale in 10^{-4} a.u.; the lines are scaled to the data.

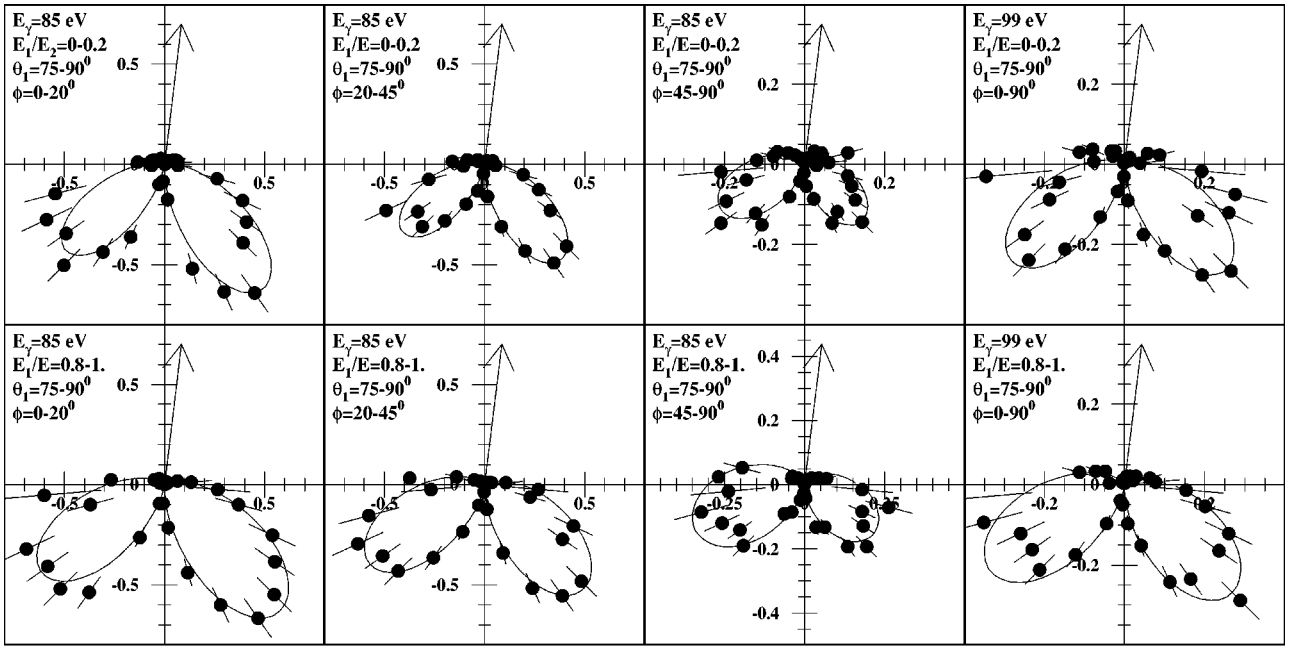

FIG. 15. $d^4\sigma/d[\cos(\vartheta_1)]d[\cos(\vartheta_2)]d\phi\, dE$ for photon energies of 85 (three left rows) and 99 eV (right row). The data for 85 eV are for energy sharing and angles as indicated in the figure, and the data for 99 eV are integrated over all azimuthal angles. Full line: fourth-order Wannier calculation. The data are on absolute scale in 10^{-4} a.u.; the lines are scaled to the data.

TABLE I. FWHM of the Gaussian fit function for equal energy sharing.

E_{exc} (eV)	FWHM (deg)	Reference
0.6 eV	67.8±3	[26]
1 eV	68.3±6	this work
1 eV	67.2±3	[26]
2 eV	80.3±2.5	[26]
4 eV	71±3	[43]
6 eV	84.7±1.2	this work
10 eV	87.13±2	[22]
18.6 eV	91±2	[43]
20 eV	91.6±2	this work
20 eV	91.0±2	[24]

ion angular distributions [48]. In that case, the FDCS $^1S^e \rightarrow {}^1P^0$ amplitude can be written

$$f(\mathbf{k}_r,\mathbf{k}_R)=\tilde{\chi}(k_r,k_R)\ [-(c_0+c_1)\ \mathbf{k}_r\cdot\hat{\mathbf{k}}_R\ \ \hat{\mathbf{k}}_R\cdot\hat{\boldsymbol{\epsilon}}+c_1\ \mathbf{k}_r\cdot\hat{\boldsymbol{\epsilon}}], \tag{10}$$

where $\tilde{\chi}(k_r,k_R)$ is an ''internal'' momentum wave function, which defines the singly differential cross section $d\sigma/dE_r$ of the recoiling ion, while the $c_{K=0,1}$ are essentially dipole excitation amplitudes of the Kth internal Wannier mode with angular-momentum projection $\mathbf{L}\cdot\hat{\mathbf{k}}_R=K$ along a body-fixed axis $\mathbf{k}_R$. The recoil-ion angular distributions derived in Ref. [48] from an expansion in bipolar harmonics are readily obtained from Eq. (10) if the vectors $\mathbf{k}_r$ and $\mathbf{k}_R$ are expressed in terms of their polar angles $\theta_\alpha,\phi_\alpha$ ($\alpha=r$ or R) relative to the photon polarization direction $\hat{\boldsymbol{\epsilon}}$. Those distributions were applied with some success in Ref. [4].

We calculate the FDCS for Figs. 11–15 when we instead introduce $\mathbf{k}_r=\mathbf{k}_1+\mathbf{k}_2$ and $\mathbf{k}_R=\frac{1}{2}(\mathbf{k}_1-\mathbf{k}_2)$ into Eq. (10), and express the conventional electron detection coordinates $\mathbf{k}_1$ and $\mathbf{k}_2$ in terms of their polar angles θ_i and ϕ_i relative to the polarization direction. The result was also given in Ref. [48] along with some sample plots. Although it agrees in form with Eq. (8), it also provides explicit expressions for a_g and a_u as functions of k_1, k_2, and θ_{12}, which appear to work equally well for most energy sharings and azimuthal angles.

The excitation amplitudes c_K in Eq. (10) have not been evaluated. Instead, we have simply parametrized the calculations in the figures in terms of the ratio c_0/c_1, and arbitrarily normalized the theory to the data. The ratio depends in principle on the excess energy E, but is independent of the momenta k_1 and k_2. Moreover, it can be related to the angular asymmetry parameters of the recoil-ion and relative electron-pair distributions β_r and β_R. Thus we fixed the Re and Im parts of c_0/c_1 for a given excess energy in all figures using beta parameters extracted from previous measurements [4,82]. Theoretical details will be presented elsewhere [83].

In Fig. 12 we illustrate the influence of the excess energy on the FDCS for equal energy sharing and the coplanar geometry. The polarization axis is horizontal and both electrons are emitted in the plane of the paper. By definition, polar angles are restricted to (0°–180°), while our azimuthal angles range from −180° to 180°. In Figs. 12–15 we display polar angles between 0° and 180° associated with azimuthal angles (−90° to 90°) in the upper half sphere and those between 0° and 180° and azimuthal angle (90°–180° and −90° to −180°) in the lower half. The acceptance ranges of ϕ chosen for Fig. 12 is $0<\phi<20°$ and $\pm 160 <\phi<\pm 180°$, respectively. For 6- and 20-eV excess energy we find a clear node in the distribution for back to back emission, but for 1 eV the node is somewhat lost by our experimental resolution. Our experiment has a constant resolution in Cartesian momentum components of the ion and one electron. Thus the angular resolution improves with excess energy. The data set shows how with decreasing excess energy the influence of the electron-electron repulsion in the final state bends the lobes more and more toward back-to-back emission. The dashed line is calculated for a Gaussian with the width given in Table I. The calculated distribution is integrated over the same range of ϑ_1 (40°–65°) and ϕ in the experimental data. We note that there is no dark area for our detectors. The experiment covers all angles. If there is no data point visible for particular angle, it coincides with the origin of the graph. At 6-eV excess energy our measured distribution is significantly narrower than the Gaussian fit. This cannot be a result of a wrong width of the Gaussian (which would tend to shift the maximum), but indicates a small deviation in shape of the correlation function from the simple assumption of a Gaussian. The shape of the Wannier calculations are, however, in excellent agreement with the data.

Our data in Figs. 12–15 are on an absolute scale. This allows for a much more stringent test of theoretical approaches. As discussed in two comparative studies [84,59] for example the 3C approach as applied to photo-double-ionization by Berakdar and co-workers [85,86] and Maulbetsch and Briggs [35–37] differs greatly in absolute height from the calculation by Pont and Shakeshaft using the 2SC approach [54,49].

As described earlier in Sec. III D, our data are consistently normalized to the same total cross section for all energy sharing and angles. Since all data are taken at once, the uncertainty in a relative comparison between the different momentum configurations at a given photon energy is smaller than the systematic uncertainty in the overall cross section. Strictly speaking, the measured FDCS's do not give the cross section at the mean value of the angular and energy range given, but the cross section averaged over the integral indicated.

Figure 13 shows data for the noncoplanar geometry. The left column gives the coplanar case. In the middle and right columns, the electron e_1 is held fixed out of the plane of the paper by 20°–45° and 45°–90°. The arrow shows the polar angle ϑ_1 which is, however, tilted out of plane. As in the previous figure azimuthal angles larger than 90° are plotted as negative ϑ_2. The main effect is on the absolute scale: the cross section drops rapidly for out-of-plane scattering. As discussed above, the emission pattern at 85-eV excess energy are very similar for all energy sharings. In the framework of the parametrization (8), this indicates that the amplitude a_u is much smaller than a_g. We find that, while for the coplanar geometry one of the lobes is strongly suppressed, they become more equal for out-of-plane geometry. As can be seen in the absolute value, this is due to a faster decrease in size of the main lobe. For equal energy sharing this behavior is well

predicted by the simple parametrization using a Gaussian correlation function. The Wannier calculation fits the shape of the FDCS very well for all energy sharings at 6 eV above threshold.

The influence of the energy sharing on the emission pattern is illustrated in Fig. 14 for 6- and 20-eV excess energy. While at the lower energy the emission pattern is almost independent of the energy sharing, we find a strong effect at the higher energy. Again the figure includes data points for all ϑ_2. We find only one lobe at this particular ϑ_1. At the low energy there is almost no back-to-back emission even for very unequal energy sharing. At 20 eV above threshold, however, back-to-back emission arises for unequal energy sharing. This was first observed by Schwarzkopf and Schmidt for the special case of $\vartheta_1=0$ [24]. It is not surprising that 20 eV above threshold for unequal energy sharing the agreement with Wannier theory is not satisfying. These configurations are far off the Wannier saddle.

For the particular case of $\vartheta_1=90°$, Maulbetsch and Briggs [41] pointed out that there is a node in the cross section at $\vartheta_2=90°$ due to the even exchange symmetry and odd parity of the final state. Schwarzkopf and co-workers (cited in Ref. [84]) measured at these angles and indeed found a node at $\vartheta_1=\vartheta_2=90°$ for the case of coplanar emission and equal energy sharing. Our data shown in the left three columns of Fig. 15 demonstrate for $E_{\mathrm{exc}}=6$ eV that this node is independent of azimuthal angle and energy sharing as well. This is not an effect of amplitude a_u in Eq. (8) being small. At $E=20$ eV we find the same effect in right column of Fig. 15. The latter data are integrated over all azimuthal angles and the node still prevails.

In conclusion, we have used COLTRIMS together with an imaging technique for electrons to obtain a comprehensive and absolute set of data on photo-double-ionization at 1, 6, and 20 eV above threshold. At all energies we find that the momentum distribution of the recoiling ion shows, contrary to the electronic momentum distribution, dipolar structure. From the same data set we also obtain an absolute FDCS for electron emission at various energy sharings and angles in the coplanar and noncoplanar geometry. As a consequence of the electronic repulsion the maximum of the cross section is, at all polar angles, at an azimuthal angle of 180° (i.e., in the coplanar geometry) between the two electrons. The data set gives an overview on the multidimensional structure of the three-body Coulomb continuum for a $^1P^0$ symmetry. We confirm the selection rules predicted by Maulbetsch and Briggs [41]. Since our data are on an absolute scale and cover a wide range of the final state phase space, they provide a link between differential studies and the extensive work on total cross sections. For the future, we would encourage theoretical work addressing the open questions of how the different mechanisms of photo-double-ionization manifest themselves in the FDCS and how initial state correlation influences the FDCS.

ACKNOWLEDGMENTS

This work was supported by BMBF, DFG, DAAD, the Max Planck Preis, and the Feodor Lynen Program of the Alexander von Humboldt Stiftung, the Studienstiftung des deutschen Volkes, DAAD, and the Division of Chemical Sciences, Office of Basic Energy Sciences, Office of Energy Research, U.S. Department of Energy. We thank the staff of the ALS for extraordinary support during our beam time and T. Warwick, E. Rothenberg, and J. Dennlinger for help with operating the beamline. It is a pleasure to thank our colleagues V. Schmidt, B. Krässig, A. Huetz, F. Maulbetsch, J. Briggs, S. Keller, J. M. Rost, R. Shakeshaft, and M. Pont for stimulating discussions, and E. Kanter and M. Jung for their help during the beam time.

[1] J. Ullrich, R. Moshammer, R. Dörner, O. Jagutzki, V. Mergel, H. Schmidt-Böcking, and L. Spielberger, J. Phys. B **30**, 2917 (1997).

[2] L. Spielberger, O. Jagutzki, R. Dörner, J. Ullrich, U. Meyer, V. Mergel, M. Unverzagt, M. Damrau, T. Vogt, I. Ali, Kh. Khayyat, D. Bahr, H. G. Schmidt, R. Frahm, and H. Schmidt-Böcking, Phys. Rev. Lett. **74**, 4615 (1995).

[3] L. Spielberger, O. Jagutzki, B. Krässig, U. Meyer, Kh. Khayyat, V. Mergel, Th. Tschentscher, Th. Buslaps, H. Bräuning, R. Dörner, T. Vogt, M. Achler, J. Ullrich, D. S. Gemmel, and H. Schmidt-Böcking, Phys. Rev. Lett. **76**, 4685 (1996).

[4] R. Dörner, J. Feagin, C. L. Cocke, H. Bräuning, O. Jagutzki, M. Jung, E. P. Kanter, H. Khemliche, S. Kravis, V. Mergel, M. H. Prior, H. Schmidt-Böcking, L. Spielberger, J. Ullrich, M. Unverzagt, and T. Vogt, Phys. Rev. Lett. **77**, 1024 (1996); **78**, 2031 (1997).

[5] R. Dörner, T. Vogt, V. Mergel, H. Khemliche, S. Kravis, C. L. Cocke, J. Ullrich, M. Unverzagt, L. Spielberger, M. Damrau, O. Jagutzki, I. Ali, B. Weaver, K. Ullmann, C. C. Hsu, M. Jung, E. P. Kanter, B. Sonntag, M. H. Prior, E. Rotenberg, J. Denlinger, T. Warwick, S. T. Manson, and H. Schmidt-Böcking, Phys. Rev. Lett. **76**, 2654 (1996).

[6] R. J. Bartlett, P. J. Walsh, Z. X. He, Y. Chung, E.-M. Lee, and J. A. R. Samson, Phys. Rev. A **46**, 5574 (1992).

[7] N. Berrah, F. Heiser, R. Wehlitz, J. Levin, S. B. Whitfield, J. Viefhaus, I. A. Sellin, and U. Becker, Phys. Rev. A **48**, R1733 (1993).

[8] J. M. Bizau and F. J. Wuilleumier, J. Electron Spectrosc. Relat. Phenom. **71**, 205 (1995).

[9] T. A. Carlson, Phys. Rev. **156**, 142 (1967).

[10] DMP. Holland, K. Codling, J. B. West, and G. V. Marr, J. Phys. B **12**, 2465 (1979).

[11] H. Kossmann, V. Schmidt, and T. Andersen, Phys. Rev. A **60**, 1266 (1988).

[12] J. C. Levin, D. W. Lindle, N. Keller, R. D. Miller, Y. Azuma, N. Berrah Mansour, H. G. Berry, and I. A. Sellin, Phys. Rev. Lett. **67**, 968 (1991).

[13] J. C. Levin, I. A. Sellin, B. M. Johnson, D. W. Lindle, R. D. Miller, N. Berrah, Y. Azuma, H. G. Berry, and D. H. Lee, Phys. Rev. A **47**, R16 (1993).

[14] J. C. Levin, G. B. Armen, and I. A. Sellin, Phys. Rev. Lett. **76**, 1220 (1996).

[15] M. Sagurton, R. J. Bartlett, J. A. R. Samson, Z. X. He, and D. Morgan, Phys. Rev. A **52**, 2829 (1995).
[16] J. A. R. Samson, Phys. Rev. Lett. **65**, 2861 (1990).
[17] J. A. R. Samson, R. J. Bartlett, and Z. X. He, Phys. Rev. A **46**, 7277 (1992).
[18] V. Schmidt, N. Sandner, H. Kuntzemüller, P. Dhez, F. Wuilleumier, and E. Käne, Phys. Rev. **13**, 1748 (1976).
[19] R. Wehlitz, F. Heiser, O. Hemmers, B. Langer, A. Menzel, and U. Becker, Phys. Rev. Lett. **67**, 3764 (1991).
[20] G. R. Wight and M. J. Van der Wiel, J. Phys. B **9**, 1319 (1976).
[21] G. Dawber, R. I. Hall, A. G. McConkey, M. A. MacDonald, and G. C. King, J. Phys. B **27**, L341 (1994).
[22] O. Schwarzkopf, B. Krässig, J. Elmiger, and V. Schmidt, Phys. Rev. Lett. **70**, 3008 (1993).
[23] O. Schwarzkopf, B. Krässig, V. Schmidt, F. Maulbetsch, and J. Briggs, J. Phys. B **27**, L347 (1994).
[24] O. Schwarzkopf and V. Schmidt, J. Phys. B **28**, 2847 (1995); **29**, 1877 (1996).
[25] A. Huetz, P. Lablanquie, L. Andric, P. Selles, and J. Mazeau, J. Phys. B **27**, L13 (1994).
[26] G. Dawber, L. Avaldi, A. G. McConkey, H. Rojas, M. A. MacDonald, and G. C. King, J. Phys. B **28**, L271 (1995).
[27] P. Lablanquie, J. Mazeau, L. Andric, P. Selles, and A. Huetz, Phys. Rev. Lett. **74**, 2192 (1995).
[28] J. Viefhaus, L. Avaldi, F. Heiser, R. Hentges, O. Gessner, A. Rüdel, M. Wiedenhöft, K. Wielczek, and U. Becker, J. Phys. B **29**, L729 (1996).
[29] J. Viefhaus, L. Avaldi, G. Snell, M. Wiedenhöft, R. Hentges, A. Rüdel, F. Schäfer, D. Menke, U. Heinzmann, A. Engelns, J. Berakdar, H. Klar, and U. Becker, Phys. Rev. Lett. **77**, 3975 (1996).
[30] Yu. F. Smirnov, A. V. Pavlitchenkov, V. G. Levin, and V. G. Neudatschin, J. Phys. B **11**, 3587 (1978).
[31] V. G. Levin, V. G. Neudatchin, A. V. Pavlitchankov, and Yu. F. Smirnov, J. Phys. B **17**, 1525 (1984).
[32] R. Moshammer, J. Ullrich, H. Kollmus, W. Schmitt, M. Unverzagt, O. Jagutzki, V. Mergel, H. Schmidt-Böcking, R. Mann, C. J. Woods, and R. E. Olson, Phys. Rev. Lett. **77**, 1242 (1996).
[33] V. Mergel, R. Dörner, M. Achler, Kh. Khayyat, S. Lencinas, J. Euler, O. Jagutzki, S. Nüttgens, M. Unverzagt, L. Spielberger, W. Wu, R. Ali, J. Ullrich, H. Cederquist, A. Salin, R. E. Olson, Dž. Belkić, C. L. Cocke, and H. Schmidt-Böcking, Phys. Rev. Lett. **79**, 387 (1997).
[34] S. Keller, H. J. Lüdde, and R. Dreizler, Phys. Rev. A **55**, 4215 (1997).
[35] F. Maulbetsch and J. S. Briggs, J. Phys. B **26**, 1679 (1993).
[36] F. Maulbetsch and J. S. Briggs, J. Phys. B **26**, L647 (1993).
[37] F. Maulbetsch and J. S. Briggs, J. Phys. B **27**, 4095 (1994).
[38] Colm Wheelan (private communication).
[39] F. W. Byron and C. J. Joachain, Phys. Rev. **164**, 1 (1967).
[40] R. Wehlitz, R. Hentges, G. Prümper, A. Farhat, T. Buslaps, N. Berrah, J. C. Levin, I. A. Sellin, and U. Becker, Phys. Rev. A **53**, R3720 (1996).
[41] F. Maulbetsch and J. S. Briggs, J. Phys. B **28**, 551 (1995).
[42] A. Huetz, P. Selles, D. Waymel, and J. Mazeau, J. Phys. B **24**, 1917 (1991).
[43] L. Malegat, P. Selles, and A. Huetz, J. Phys. B **30**, 251 (1997); L. Malegat, P. Selles, P. Lablanquie, J. Mazeau, and A. Huetz, *ibid.* **30**, 263 (1997).
[44] A. K. Kazanski and V. N. Ostrovsky, J. Phys. B **28**, 1453 (1995).
[45] A. K. Kazanski and V. N. Ostrovsky, Phys. Rev. A **51**, 3698 (1995).
[46] G. H. Wannier, Phys. Rev. **90**, 817 (1953).
[47] J. M. Feagin, J. Phys. B **28**, 1495 (1995).
[48] J. M. Feagin, J. Phys. B **29**, l551 (1996).
[49] M. Pont and R. Shakeshaft, Phys. Rev. A **54**, 1448 (1996).
[50] J. H. McGuire, N. Berrah, R. J. Bartlett, J. A. R. Samson, J. A. Tanis, C. L. Cocke, and A. S. Schlachter, J. Phys. B **28**, 913 (1995).
[51] A. Dalgarno and H. R. Sadeghpour, Phys. Rev. A **46**, R3591 (1992).
[52] Ken-ichi Hino, T. Ishihara, F. Shimizu, N. Toshima, and J. H. McGuire, Phys. Rev. A **48**, 1271 (1993).
[53] Z. J. Teng and R. Shakeshaft, Phys. Rev. A **49**, 3597 (1994).
[54] M. Pont and R. Shakeshaft, Phys. Rev. A **51**, R2676 (1995).
[55] A. K. Kazanski and V. N. Ostrovsky, Phys. Rev. A **48**, R871 (1993).
[56] A. K. Kazanski and V. N. Ostrovsky, J. Phys. B **27**, 447 (1994).
[57] F. Maulbetsch, M. Pont, J. S. Briggs, and R. Shakeshaft, J. Phys. B **28**, L341 (1995).
[58] M. Pont and R. Shakeshaft, Phys. Rev. A **51**, 494 (1995).
[59] M. Pont, R. Shakeshaft, F. Maulbetsch, and J. S. Briggs, Phys. Rev. A **53**, 3671 (1996).
[60] R. Dörner, V. Mergel, R. Ali, U. Buck, C. L. Cocke, K. Froschauer, O. Jagutzki, S. Lencinas, W. E. Meyerhof, S. Nüttgens, R. E. Olson, H. Schmidt-Böcking, L. Spielberger, K. Tökesi, J. Ullrich, M. Unverzagt, and W. Wu, Phys. Rev. Lett. **72**, 3166 (1994).
[61] R. Moshammer, J. Ullrich, M. Unverzagt, W. Schmidt, P. Jardin, R. E. Olson, R. Mann, R. Dörner, V. Mergel, U. Buck, and H. Schmidt-Böcking, Phys. Rev. Lett. **73**, 3371 (1994).
[62] V. Mergel, R. Dörner, J. Ullrich, O. Jagutzki, S. Lencinas, S. Nüttgens, L. Spielberger, M. Unverzagt, C. L. Cocke, R. E. Olson, M. Schulz, U. Buck, E. Zanger, W. Theisinger, M. Isser S. Geis, and H. Schmidt-Böcking, Phys. Rev. Lett. **74**, 2200 (1995).
[63] W. Wu, R. Ali, C. L. Cocke, V. Frohne, J. P. Giese, B. Walch, K. L. Wong, R. Dörner, V. Mergel, H. Schmidt-Böcking, and W. E. Meyerhof, Phys. Rev. Lett. **72**, 3170 (1994).
[64] V. Frohne, S. Cheng, R. Ali, M. Raphaelian, C. L. Cocke, and R. E. Olson, Phys. Rev. Lett. **71**, 696 (1993).
[65] R. Ali, V. Frohne, C. L. Cocke, M. Stöckli, S. Cheng, and M. L. A. Raphaelian, Phys. Rev. Lett. **69**, 2491 (1992).
[66] R. Dörner, V. Mergel, L. Zhaoyuan, J. Ullrich, L. Spielberger, R. E. Olson, and H. Schmidt-Böcking, J. Phys. B **28**, 435 (1995).
[67] R. Dörner, T. Vogt, V. Mergel, H. Khemliche, S. Kravis, C. L. Cocke, J. Ullrich, M. Unverzagt, L. Spielberger, M. Damrau, O. Jagutzki, I. Ali, B. Weaver, K. Ullmann, C. C. Hsu, M. Jung, E. P. Kanter, B. Sonntag, M. H. Prior, E. Rotenberg, J. Denlinger, T. Warwick, S. T. Manson, and H. Schmidt-Böcking, Phys. Rev. Lett. **77**, 4520 (1996).
[68] M. Unverzagt, R. Moshammer, W. Schmitt, R. E. Olson, P. Jardin, V. Mergel, J. Ullrich, and H. Schmidt-Böcking, Phys. Rev. Lett. **76**, 1043 (1996).
[69] A. Cassimi, S. Duponchel, X. Flechard, P. Jardin, P. Sortais,

D. Hennecart, and R. E. Olson, Phys. Rev. Lett. **76**, 3679 (1996).
[70] T. Kambara, J. Z. Tang, Y. Awaya, B. D. dePaola, O. Jagutz, Y. Kanai, M. Kimura, T. M. Kojima, V. Merg, H. W. Schmidt-Böcking, and I. Shimamura, J. Phys. B **28**, 4593 (1995).
[71] G. Brusdeylins, J. P. Toennies, and R. Vollmer, *XII International Symposium on Molecular Beams*, edited by V. Aquilanti (University of Perugia, Perugia, 1989), p. 98.
[72] V. Mergel, *Dynamische Elektron Korrelation in Helium* (Shaker Verlag, Aachen, 1996).
[73] D. Proulx and R. Shakeshaft, Phys. Rev. A **48**, R875 (1993).
[74] J. A. R. Samson, Z. X. He, L. Yin, and G. N. Haddad, J. Phys. **27**, 887 (1993).
[75] J. A. R. Samson, W. C. Stolte, Z. X. He, J. N. Cutler, and Y. Lu (unpublished).
[76] V. Schmidt, Rep. Prog. Phys. **55**, 1483 (1992).
[77] R. Wehlitz, B. Langer, N. Berrah, S. B. Whitfield, and U. Becker, J. Phys. B **26**, L783 (1993).
[78] V. Schmidt, H. Derenbach, and R. Malutzki, J. Phys. **15**, L523 (1982).
[79] J. M. Bizeau, F. Wuilleumier, P. Dhez, D. L. Ederer, T. N. Chang, S. Krummacher, and V. Schmidt, Phys. Rev. Lett. **48**, 588 (1982).
[80] J. M. Feagin and J. S. Briggs, Phys. Rev. Lett. **57**, 984 (1986).
[81] V. Schmidt, in *Atomic and Molecular Photoionization*, edited by A. Yagishita and T. Sazaki (Universal Academy Press, Tokyo, 1996), p. 21.
[82] H. P. Bräuning, R. Dörner, C. L. Cocke, M. H. Prior, B. Krässig, A. Bräuning-Demian, K. Carnes, S. Dreuil, V. Mergel, P. Richard, J. Ullrich, and H. Schmidt-Böcking, J. Phys. B **30**, L649 (1997).
[83] J. M. Feagin, J. Phys. B (to be published).
[84] F. Maulbetsch, M. Pont, J. S. Briggs, and R. Shakeshaft, J. Phys. B **28**, L341 (1995).
[85] J. Berakdar and H. Klar, Phys. Rev. Lett. **69**, 1175 (1992).
[86] J. Berakdar, H. Klar, A. Huetz, and P. Selles, J. Phys. B **26**, 1463 (1993).